Reversal of Anomalous Hall Effect and Octahedral Tilting in SrRuO 3 Thin Films via Hydrogen Spillover

Hyeon Han, Hua Zhou, Charles Guillemard, Manuel Valvidares, Arpit Sharma, Yan Li, Ankit K Sharma, Ilya Kostanovskiy, Arthur Ernst, Stuart S P Parkin

ADVANCED MATERIALS
www.advmat.de

Reversal of Anomalous Hall Effect and Octahedral Tilting in $SrRuO_3$ Thin Films via Hydrogen Spillover

Hyeon Han, Hua Zhou, Charles Guillemard, Manuel Valvidares, Arpit Sharma, Yan Li, Ankit K. Sharma, Ilya Kostanovskiy, Arthur Ernst, and Stuart S. P. Parkin**

The perovskite $SrRuO_3$ (SRO) is a strongly correlated oxide whose physical and structural properties are strongly intertwined. Notably, SRO is an itinerant ferromagnet that exhibits a large anomalous Hall effect (AHE) whose sign can be readily modified. Here, a hydrogen spillover method is used to tailor the properties of SRO thin films via hydrogen incorporation. It is found that the magnetization and Curie temperature of the films are strongly reduced and, at the same time, the structure evolves from an orthorhombic to a tetragonal phase as the hydrogen content is increased up to ≈0.9 H per SRO formula unit. The structural phase transition is shown, via in situ crystal truncation rod measurements, to be related to tilting of the RuO_6 octahedral units. The significant changes observed in magnetization are shown, via density functional theory (DFT), to be a consequence of shifts in the Fermi level. The reported findings provide new insights into the physical properties of SRO via tailoring its lattice symmetry and emergent physical phenomena via the hydrogen spillover technique.

1. Introduction

The anomalous Hall effect (AHE) is one of the most intriguing transport phenomena in magnetic materials, where the effect typically stems from the interplay between magnetic-ordering and spin–orbit coupling. Diverse applications such as magnetic memories, sensors, and energy-efficient spintronic devices are proposed due to the high sensitivity and stability of the anomalous Hall signal.[1–4] Another fascinating transport phenomenon in magnetic systems is the topological Hall effect (THE) which is often assumed to reflect the presence of skyrmionic like objects.[5–8] $SrRuO_3$ (SRO) is a strongly correlated perovskite that is ferromagnetic below ≈150 K.[9] It was proposed from the observation of a THE in thin films that skyrmions might be present in SRO[10–15] but it was later reported that these features are likely due to multiple AHE contributions from inhomogeneities in the thin films.[16–22] The sign of the AHE has been shown to depend, in thin SRO layers, on the film thickness, the magnetization, and chemical potential, which was attributed to a competition between different Berry curvature sources in the multiple nodal band structure.[23]

Hydrogenation (protonation) is a means of inducing significant changes in the physical property of correlated oxides owing to its light weight, small size, and high ionic mobility. Diverse applications have been proposed, such as proton-gated electronic devices,[24,25] synaptic plasticity,[25–27] spintronic devices,[28,29] sensors,[30] and fuel cells.[31] Various methods have been used to carry out the hydrogenation that include hydrogen spillover,[27,28,32–35] electrolyte gating,[24–26] and ionic liquid gating.[29,36–38] Ionic liquid gating of an oxide layer involves the formation of an electric double layer at the surface with large electric fields that can result in significant electrostatic tuning of the carrier charge density[39] but which can also lead to oxygen vacancy formation,[40–42] as well as hydrogen intercalation that typically arises from water dissolved in the ionic liquid. [36–38] Therefore, to unambiguously unravel the effect of hydrogen on the physical property of SRO films, a method that introduces hydrogen alone is desired. Here, we demonstrate the use of such a technique, namely hydrogen spillover, that results in significant changes in the structural, electronic, magnetic, and transport properties of SRO thin films.

H. Han, A. Sharma, A. K. Sharma, I. Kostanovskiy, A. Ernst, S. S. P. Parkin
Nano Systems from Ions, Spins, and Electrons (NISE)
Max Planck Institute of Microstructure Physics
06120 Halle (Saale), Germany
E-mail: hyeon.han@mpi-halle.mpg.de; stuart.parkin@mpi-halle.mpg.de

H. Zhou
Advanced Photon Source
Argonne National Laboratory
Lemont, IL 60439, USA

C. Guillemard, M. Valvidares
ALBA Synchrotron Light Source
Cerdanyola del Vallès, Barcelona E-08290, Spain

Y. Li
Materials Science Division
Argonne National Laboratory
Lemont, IL 60439, USA

A. Ernst
Institute for Theoretical Physics
Johannes Kepler University
Linz 4040, Austria

The ORCID identification number(s) for the author(s) of this article can be found under https://doi.org/10.1002/adma.202207246.

DOI: 10.1002/adma.202207246

A specially designed in situ hydrogenation system is employed to insert hydrogen while monitoring the resistance changes of SRO films. For a film that is 4.5 nm thick, we find that hydrogenation leads to a metal–insulator transition, a decrease in magnetism, and a sign reversal of the AHE. In addition, in situ synchrotron X-ray diffraction measurements reveal a corresponding structural phase transformation from an initial orthorhombic phase to a tetragonal structure due to tilting of the RuO_6 octahedra. Density functional theory (DFT) calculations show distinct changes in magnetic properties and a shift in the Fermi level. Moreover, the emergence of THE-like features when the hydrogenated thin film is exposed to air, suggests that their formation is a result of the coexistence of two phases with opposite AHE signals rather than any intrinsic contribution from non collinear spin textures.

2. Results and Discussion

2.1. Transport Property Changes via Hydrogen Spillover

The epitaxial SRO thin films used in this study were grown on $SrTiO_3$ (STO) (001) substrates using pulsed laser deposition (PLD). Most studies were carried out on several films, each 4.5 nm thick. The film structure was characterized by θ–2θ X-ray diffraction (XRD) and reflection high-energy electron diffraction (RHEED) (Figure S1, Supporting Information). Hall bar geometry devices (Figure S2, Supporting Information) were fabricated using conventional photolithography techniques for the transport studies. Pt nanoparticles, as a catalyst for the hydrogen spillover, were then deposited on the device using a high-pressure sputter coater (**Figure 1**a and the Experimental Section). A purpose-built hydrogenation system which allowed for the in situ monitoring of the sample's resistance was fabricated (Figure 1b and Figure S3, Supporting Information) within the sample puck of a Quantum Design Physical Property Measurement System (PPMS). A continuous flow of a gas mixture of 5% H_2–95% Ar was used to hydrogenate the device at a hydrogenation temperature T_h that varied from 90 to 190 °C. Detailed experimental procedures are given in the Experimental Section.

Figure 1b summarizes the evolution of the normalized resistance of a 4.5 nm-thick SRO film during hydrogenation at T_h = 120 °C. The pristine film exhibits a negative AHE ($\rho_{AHE} < 0$), while the fully hydrogenated film shows a positive AHE ($\rho_{AHE} > 0$) (Figure 1c). Note that the Pt nanoparticles do not affect the AHE signal. That is, the AHE signal of the device does not show any noticeable change after deposition of the Pt (Figure S4, Supporting Information). Hydrogenation also results in a structural change from an orthorhombic to a tetragonal crystal structure that is discussed in detail below.

Temperature-dependent electrical resistivity (ρ_{xx}–T) curves (**Figure 2**a) of a 4.5 nm-thick SRO film show an increase in ρ_{xx} with increasing hydrogenation temperature (T_h), evolving from metallic to an insulating behavior for T_h = 190 °C. The Curie temperature (T_C), obtained from the peak in the first derivative of the $\rho_{xx}(T)$ curve (Figure S5, Supporting Information), decreases with increasing T_h. Hall resistivity (ρ_{xy}) curves for the pristine and hydrogenated films are shown in Figure S6,

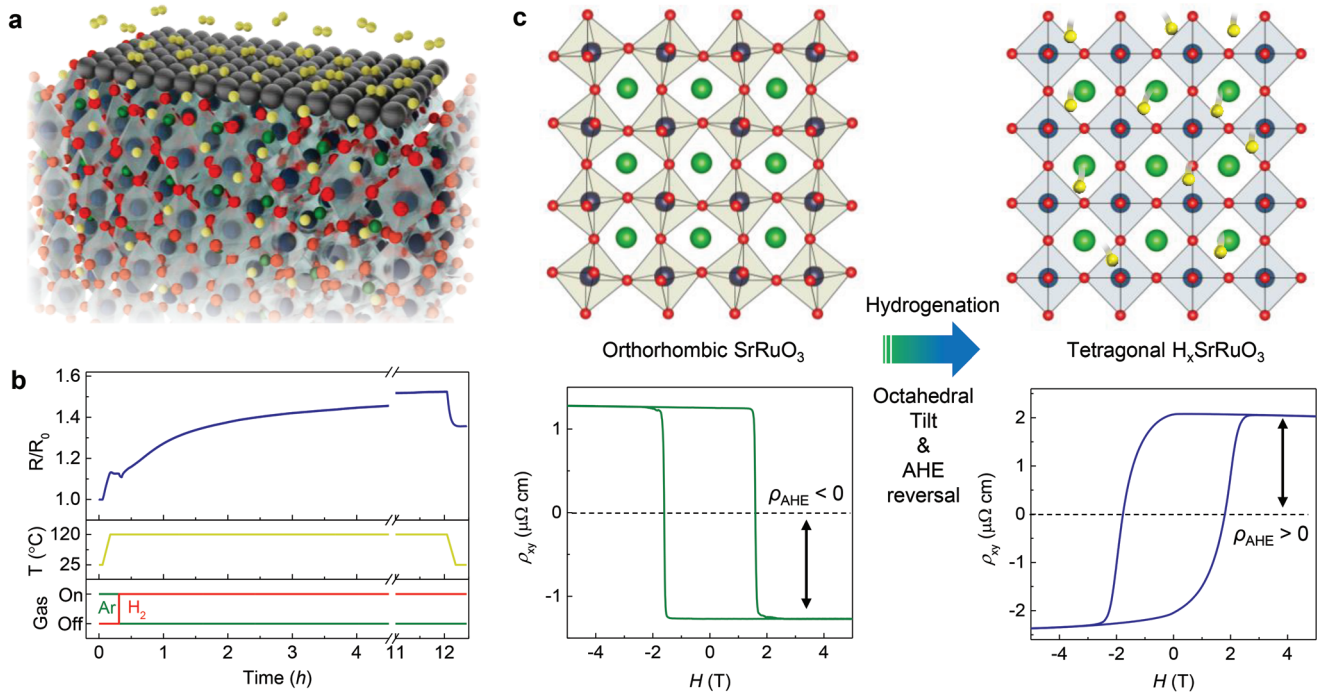

Figure 1. Hydrogenation of $SrRuO_3$ thin films via hydrogen spillover. a) Schematic figure of hydrogen intercalation into the $SrRuO_3$ lattice via a hydrogen spill over method. The black, green, navy, red, and yellow spheres denote Pt, Sr, Ru, O, and H ions, respectively. b) Time-dependent changes in resistance, temperature, and gas flow during the in situ hydrogen spillover process. c) A scheme of hydrogenation of $SrRuO_3$ thin films, revealing reversal of AHE along with a lattice change from orthorhombic to tetragonal accompanied by the octahedral tilt. The green, navy, red, and yellow spheres indicate Sr, Ru, O, and H ions, respectively.

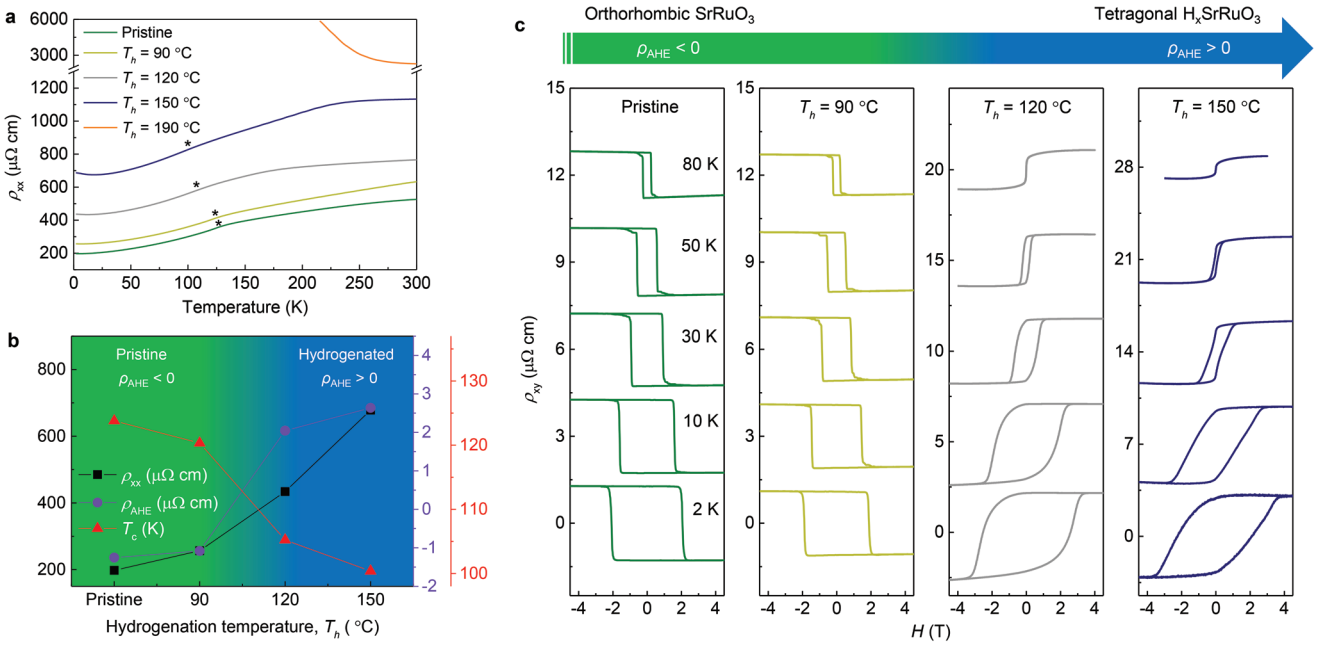

Figure 2. Transport properties of $SrRuO_3$ thin films via hydrogenation. a) Electrical resistivity–temperature (ρ_{xx}–T) curves for different hydrogenation temperatures (T_h). b) T_h-dependent electrical resistivity (ρ_{xx}) at 10 K, anomalous Hall resistivity (ρ_{AHE}) at 10 K, and Curie temperature (T_C). c) Hall resistivity (ρ_{xy}) curves measured at low temperatures (2, 10, 30, 50, and 80 K) for the pristine and hydrogenated SRO.

Supporting Information. By subtracting the linear background contribution from the ordinary Hall effect, the anomalous Hall resistivity (ρ_{AHE}) was obtained, as shown in Figure 2c. Figure 2b summarizes the dependence of ρ_{xx} and ρ_{AHE} at 10 K, and T_C as a function of T_h. The pristine and T_h = 90 °C films show a negative AHE at low temperatures, whereas, the T_h = 120 and 150 °C films exhibit a positive AHE. The T_h = 190 °C film shows no AHE, indicative of a transition to a paramagnetic state (Figure S7, Supporting Information).

Transport measurements as a function of SRO film thickness after hydrogenation at 120 and 190 °C (Figure S8, Supporting Information) show that the 3 nm-thick film undergoes a metal-to-insulator transition at low temperatures, whereas the 12 nm-thick film does not show a reversal in the sign of the AHE. This suggests that the 3 nm-thick film is completely hydrogenated at 120 °C, whereas the 12 nm-thick film is incompletely hydrogenated even at 190 °C. For these reasons, the 4.5 nm-thick film was chosen for most of the experiments. Both the 4.5 and 12 nm-thick films show good crystallinity even after hydrogenation at high temperatures (Figure S9, Supporting Information). Detailed structural analyses will be presented in later sections.

2.2. Electronic, Magnetic, and Chemical Property Changes via Hydrogenation

The magnetic properties are investigated by temperature-dependent magnetization (M–T curves) and field-dependent magnetization hysteresis (M–H curves) measurements, using a superconducting quantum interference device (SQUID) magnetometer (**Figure 3**a and Figure S10, Supporting Information). As T_h is increased, both M and T_C decrease, while the coercivity (H_c) increases.

X-ray absorption spectroscopy (XAS) and X-ray magnetic circular dichroism (XMCD) measurements were performed to further investigate the electronic and magnetic structural changes via hydrogenation (Figure 3b–d). O K-edge XAS spectra show a decrease in the absorption peak at ≈530 eV with increasing T_h (Figure 3b). This absorption peak was previously shown to be related to an electronic state formed from the hybridization of the O 2p and Ru 4d t_{2g} orbitals.[43] Figures 3c,d show XAS spectra at the Ru $L_{2,3}$-edges and the corresponding XMCD signals, respectively, obtained from the difference between the XAS acquired with right-handed and left-handed circular polarizations, respectively. A clear and progressive reduction of the XMCD signal is observed with increasing T_h. Estimates of the orbital and spin elemental moments can be extracted using the XMCD sum rules (see Figure S11, Supporting Information).[44] The Ru magnetic moment for the pristine SRO sample is ≈1.0 μ_B Ru^{-1}, and is lowered to ≈0.5 and ≈0.4 μ_B Ru^{-1} for T_h = 120 and 150 °C, respectively.

X-ray photoelectron spectroscopy (XPS) was carried out to explore the chemical property changes induced by hydrogen spillover (Figure S12, Supporting Information). Although it is a surface sensitive technique, we can follow the relative changes in the chemical state. The O 1s spectra can be deconvoluted into three peaks, with increasing binding energy, corresponding to oxygen bound to the lattice, oxygen defects/vacancies, and the formation of hydroxyl (O—H) groups.[45,46] Notably, a significant increase in the hydroxyl peak after hydrogenation is found, while the O defect peak is not noticeably changed, indicating that hydrogen intercalation is dominant over oxygen vacancy formation.

The hydrogen gas for the spillover process was replaced with a mixture of 5% deuterium (D_2) and 95% Ar gas so that elastic recoil detection (ERD) spectroscopy could be carried out to determine the amount of hydrogen introduced into the SRO

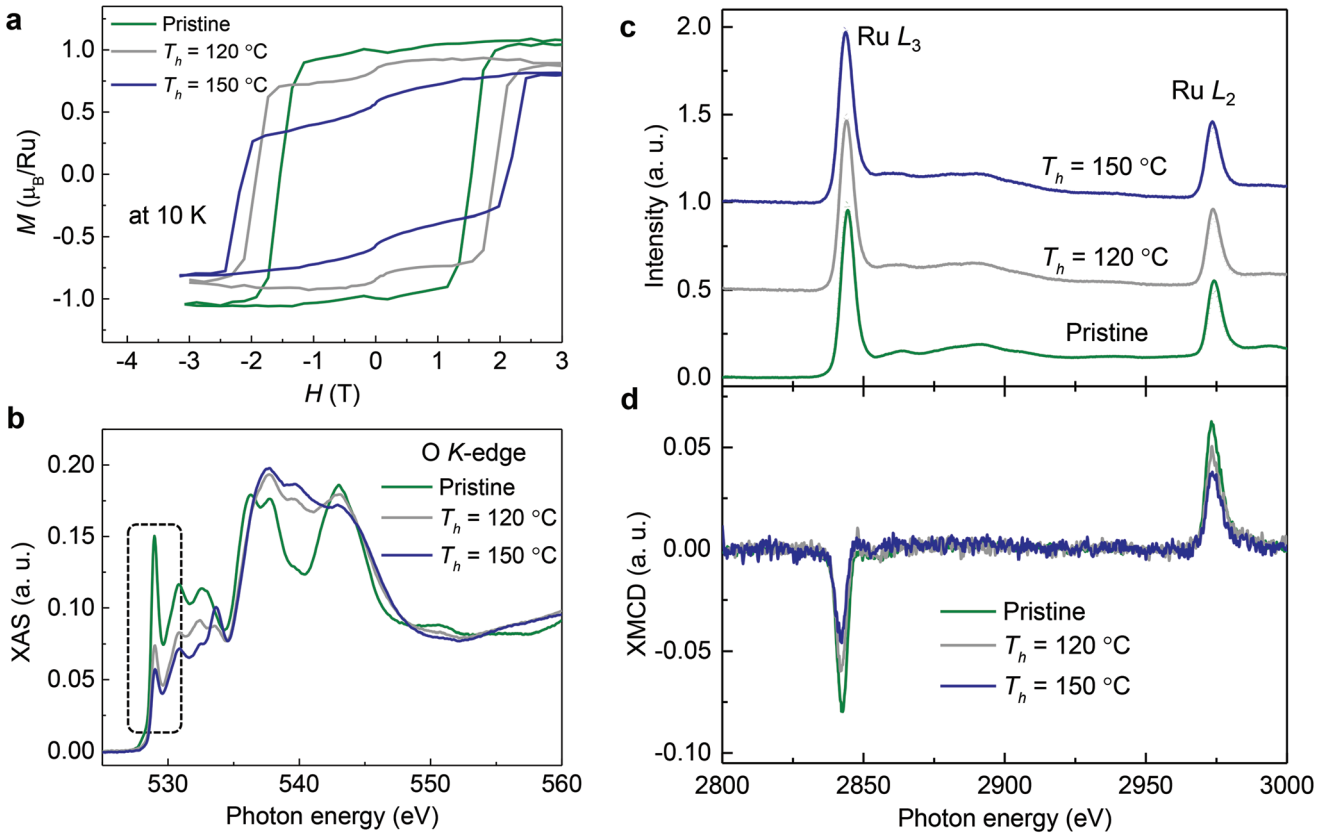

Figure 3. Electronic and magnetic properties of the hydrogenated $SrRuO_3$ thin films. a) Magnetic field (H)–magnetization (M) hysteresis curves measured by the SQUID magnetometer at 10 K. b) O K-edge XAS spectra showing a significant difference between the pristine and hydrogenated samples at ≈530 eV. c) Ru-$L_{2,3}$ XAS spectra and d) the corresponding XMCD spectra evidencing a decrease of magnetization with hydrogenation.

sample. A result for T_h = 150 °C is shown in Figure S13, Supporting Information. The use of deuterium enables the natural hydrogen signal on the film surface to be eliminated. The Sr and Ru contents were determined from Rutherford backscattering spectrometry (RBS) measurements. The composition of the film was thereby determined to be about $D_{0.9}SrRuO_3$ confirming that a large amount of D was introduced into the entire volume of the film. The error bar in the D concentration was estimated to be ±7 at%.

2.3. In Situ Synchrotron X-ray Diffraction Measurements During Hydrogenation

To explore the origin of the change in sign of the AHE resulting from hydrogenation, the structure of the SRO thin film during the H spillover treatment was studied by in situ synchrotron X-ray diffraction (XRD) studies (at the Pohang Accelerator Laboratory). **Figure 4**a shows the time-dependent evolution of the two distinct (003) reflections that correspond to the SRO film and the STO substrate, respectively, at T_h = 120 °C. The lattice expands, whereby the out-of-plane lattice constant increases by about 1% from ≈3.99 Å saturating at a value of ≈4.03 Å, after ≈30 min. Then, when the hydrogen is replaced by dry air (after ≈10 h) at the same temperature, the out-of-plane lattice parameter decreases back to its original value (≈3.99 Å), which takes a longer time of ≈1.5 h.

A second SRO film structure was separately analyzed using in situ crystal truncation rod (CTRs) measurements in an experiment at the Advanced Photon Source (Figure 4b and Figure S14, Supporting Information). This measurement exploits interference between scattering from the film structure with that from the substrate, according to $F_{tot}(hkl) = F_{sub} + F_{film}\exp[i\varphi]$, where F_{sub} and F_{film} represent the structure factors of a given (hkl) reflection from the substrate and the film. φ is a phase factor. These measurements show clear evidence for an increase in the lattice symmetry from orthorhombic to tetragonal after hydrogenation at T_h = 120 °C. Fractional order reflections appear as a result of both in-plane rotation and out-of-plane tilting of the RuO_6 octahedra, which involves the formation of a (2 × 2 × 2) superstructure relative to the (pseudocubic) (1 × 1) unit cell. Following the notation by Glazer,[47] this rotation/tilt system is labeled as $a^{\delta-}a^{\delta-}c^{-}$ for the orthorhombic structure which is modified to $a^0a^0c^-$ when the symmetry of the lattice is transformed into tetragonal. Half-order reflections are observed along all three lattice directions in reciprocal space.

2.4. Effect of Octahedral Tilt on the AHE Sign

To distinguish whether the observed AHE sign reversal originates from the change in lattice symmetry or from tuning of the chemical potential via hydrogen doping, we explored the AHE

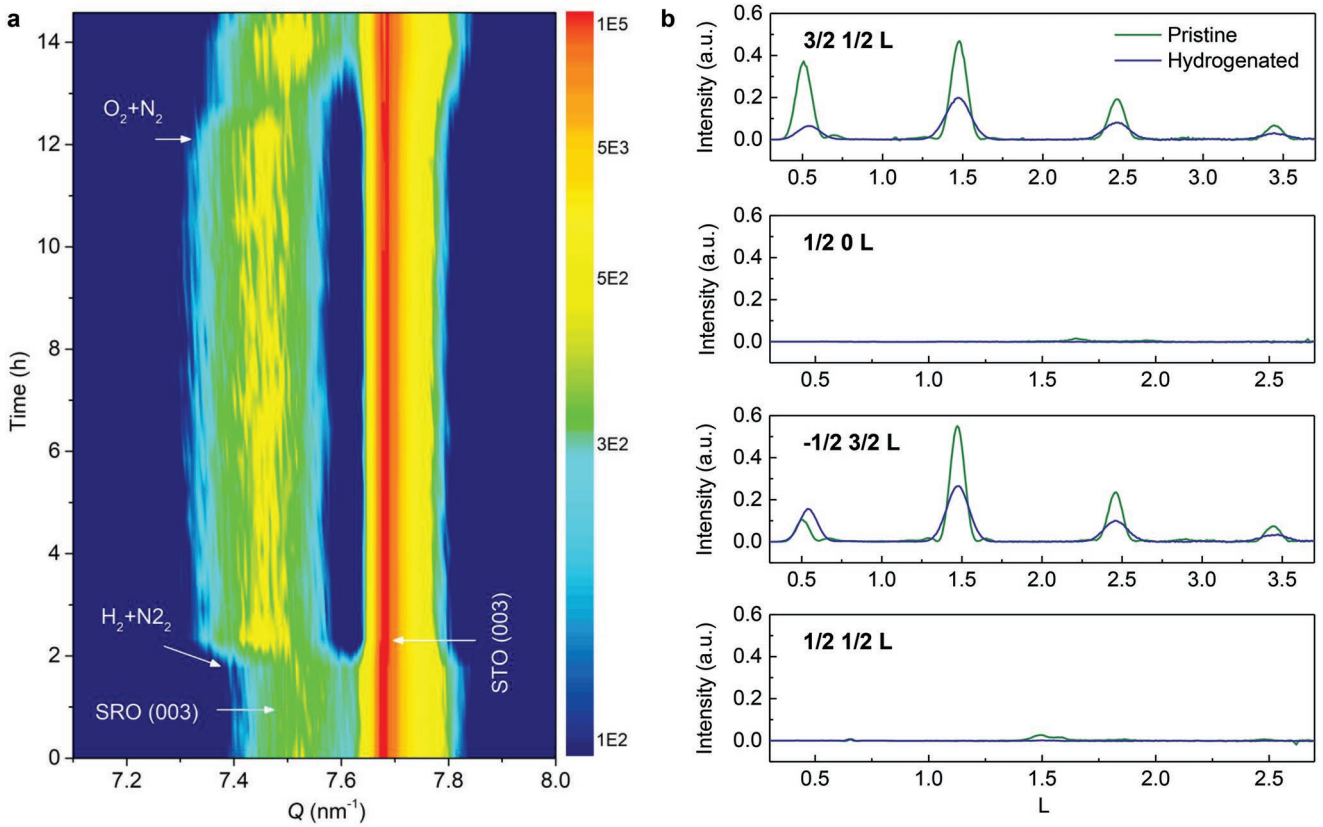

Figure 4. In situ synchrotron X-ray diffraction measurements and crystal truncation rod (CTRs) measurements during hydrogenation. a) Time-dependent evolution of the (003) reflection intensities during hydrogenation and dehydrogenation as indicated by the labels that show when first a 5 at% H_2+N_2 mixture was introduced and afterward a mixture of 21 at% O_2+N_2. Hydrogenation is related to an expansion of the *c*-lattice parameter as evidenced by the shift of the SRO (003) reflection position relative to STO (003). The measurements were carried out at 120 °C. b) Crystal truncation rod (CTRs) measurements before and after in situ hydrogenation, in this case using a 3 at% H_2+Ar mixture for 12 h at 120 °C. Intensity of octahedral tilting induced half-order reflections for the pristine and the hydrogenated SRO film. Octahedral distortion both in-plane and out-of-plane induce the appearance of a pseudocubic (2×2×2) superstructure reflected in half order spots along all reciprocal lattice directions. Hydrogenation strongly reduces the intensity of these reflections as a result of the transition from the orthorhombic lattice symmetry of the pristine film characterized by the tilt system $a^{\delta-}a^{\delta-}c^{-}$ to the teragonal lattice symmetry with the tilt system characterized by $a^0a^0c^{-}$.

of tetragonal films. The tetragonal SRO films can be grown by using low oxygen pressure,[13,48,49] using a buffer layer,[50,51] or by applying a substrate-induced strain.[52,53] We fabricated 4.5 nm- and 20 nm-thick tetragonal SRO thin films on STO (001) substrates by using a reduced oxygen pressure (1 mTorr) during the film deposition.[48,49] From reciprocal space mapping (RSM) measurements (Figure S15, Supporting Information), the orthorhombic film (grown at 100 mTorr) shows a change in the SRO {103} peak positions due to an octahedral tilt,[48–50] while the tetragonal film (grown at 1 mT) shows unchanged peak positions for the {103} reflections. In addition, the magnetization versus temperature curves (Figure S16, Supporting Information) show isotropic and anisotropic in-plane magnetic behavior for the orthorhombic and tetragonal films, respectively.[48–50] It has been reported that the tetragonal film exhibit a change in AHE sign with increasing film thickness,[13] which we also find in our films (Figure S17, Supporting Information). Notably, the 4.5 nm-thick tetragonal film exhibits a negative AHE, thereby indicating that the AHE sign reversal via hydrogenation (Figure 2c) is due to the hydrogen intercalation effect (chemical potential change) rather than the tetragonal distortion.

2.5. Dehydrogenation Process

The dehydrogenation process in air or in an oxygen environment can lead to a reversal of physical properties, that is, VO_2 thin films show reversible electrical resistivity changes via hydrogenation/dehydrogenation.[32] In contrast, the SRO films show an increase in resistivity for both hydrogenation and dehydrogenation processes (Figure S18, Supporting Information) even though the dehydrogenation leads to a decrease in the hydrogen concentration (Figure S12, Supporting Information), and the lattice parameters change back to the original state (Figure 4a). In the case of the Hall resistivity, the THE-like hump signal is shown when the film is exposed to air for intermediate times of ≈1 h, while AHE reverses back after longer exposures to air (≈2 h). The intermediate signal can be due to a mixture of the orthorhombic and hydrogenated tetragonal phases or the formation of a new phase during dehydrogenation. Identifying the dehydrogenation mechanism is beyond the scope of this study. Nevertheless, from the in situ synchrotron XRD measurements during the dehydrogenation process, no new phase is observed (Figure S19, Supporting

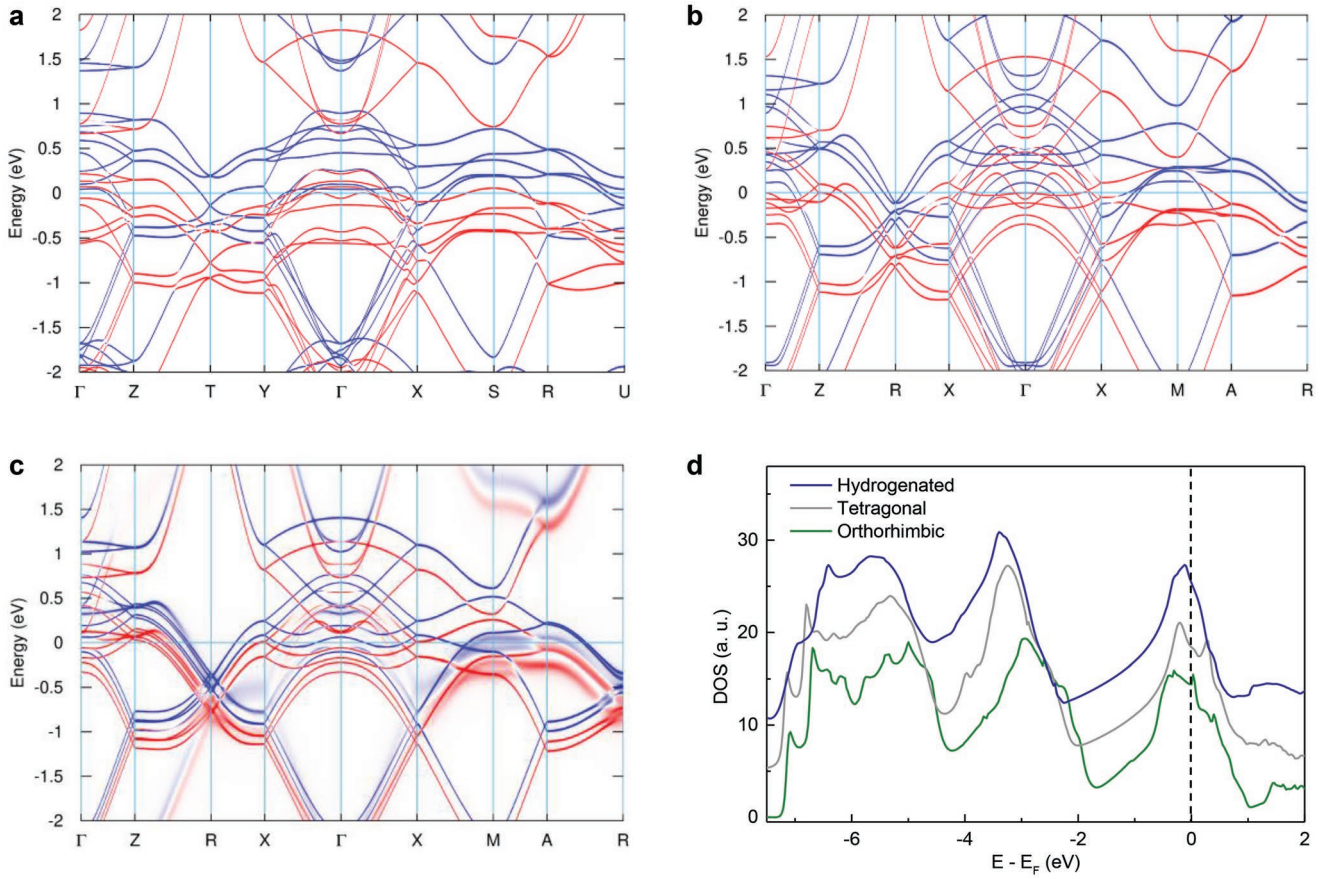

Figure 5. First-principles calculations of SRO via hydrogenation. a–c) Relativistic spin polarized band structures of the orthorhombic (a), tetragonal (b), and hydrogenated tetragonal (c) SRO phases. The red and blue colors denote spin up and spin down states, respectively. d) Density of states (DOS) of the orthorhombic, tetragonal, and hydrogenated SRO phase.

Information). In addition, the possibility that the intermediate AHE signal was a result of magnetic skyrmion-like structures was ruled out by magnetic force microscopy (MFM) measurements of a $T_h = 120$ °C film that was exposed to air for 1 h (see Figure S20, Supporting Information).

2.6. First-Principles Calculations of Hydrogenated $SrRuO_3$

We performed first-principles calculations to explore the effect of hydrogenation on the electronic band structure and magnetic structure. We consider first the two cases: pristine SRO in the orthorhombic (**Figure 5**a) and tetragonal phases without any hydrogen (Figure 5b). In accord with our experiments, the SRO is ferromagnetic in both phases with calculated magnetic moments of $\mu_{Ru}^{O} = 1.13\mu_B$ in the orthorhombic phase and $\mu_{Ru}^{T} = 0.82\mu_B$ in the tetragonal phase. The reduction of the magnetic moment in the latter case can be attributed to a strong reduction of the density of states (DOS) at the Fermi level.[54] Next, we simulated the tetragonal SRO phase found in our experiment after hydrogen doping by assuming the observed structural relaxations and by changing the hydrogen concentration from $x = 0$ (pristine) to $x = 0.75$ ($H_{0.75}SrRuO_3$). The Ru magnetic moment was then found to increase from $\mu_{Ru}^{T} = 0.82\mu_B$ to $\mu_{Ru}^{T} = 0.93\mu_B$ upon the structural relaxation for $x = 0$. However, hydrogen doping ($x = 0.75$) acts as an electron dopant and thereby shifts the DOS down in energy (Figures 5c,d). This substantially reduced the size of the Ru magnetic moment from $\mu_{Ru}^{T} = 0.93\mu_B$ to $\mu_{Ru}^{T} = 0.52\mu_B$, and the spin polarization is decreased as the DOS at the Fermi level shrinks. This affects the exchange interaction between the Ru moments, in this case, via a Ruderman–Kittel–Kasuya–Yosida (RKKY) interaction.

Upon hydrogen doping, the band structure experiences the following modifications which affect the AHE in this system. First, a shift of the DOS down in energy reduces the Ru magnetic moments and thereby the overall magnetization. The spin splitting of the bands is reduced significantly, and the shape of the bands is also modified. The bands in the Γ–*X* and *X*–*M* directions are shifted away from the Fermi level. This should decrease the conductivity and together with the magnetization reduction may account for the change in the AHE sign. However, the hydrogen doping not only leads to a shift in the DOS but the hydrogen valence states are located close to the Fermi level and hybridize with the 4d states of Ru, especially along the *X*–*M* and *M*–*R* directions. This can be clearly be seen as a broadening in the spectral functions in this part of the Brillouin Zone and the separation of the Ru 4d bands at the *M* point. The most important outcome is the lifting of the degeneracy of the nodal points or lines at the *M* point and in

its vicinity, as earlier reported by Sohn et al.[23] In addition, the hybridization between H sp and Ru 4d states modifies strongly the shape of the bands along the Γ–*X* direction. These bands are no longer parabolic.

3. Conclusion

Our observation of a change in the lattice of SRO films to a higher symmetry and an AHE sign reversal for 4.5 nm-thick films by the hydrogen spillover is distinct from ILG of thicker films (≈30 nm) that show symmetry lowering and an emergent THE signal via hydrogen incorporation.[29] In contrast, ultrathin (4–5 unit cells) SRO films have shown a sign reversal of AHE via ILG, which is explained by a change in the chemical potential.[23] However, as ILG involves complex mechanisms such as an electrostatic effect, oxygen vacancy formation, and hydrogen intercalation, it is challenging to distinguish each contribution to the physical property changes. The use of Pt nanoparticles to catalyze hydrogenation in thin films of correlated electron oxides is shown to be a powerful tool to modify properties of such films non-electrostatically. We have demonstrated that the lattice symmetry and the electronic and magnetic properties of SRO thin films are significantly affected by the incorporation of hydrogen that results in an increase in resistivity, a decrease in the magnetization and Curie temperature, and a sign reversal of the AHE, as well as a structural change resulting from tilting of the RuO_6 octahedra. Thus, our results provide new insights into the emergent phenomena in SRO thin films and suggests a novel concept to tailor the lattice symmetry and the associated exotic physical properties in strongly correlated systems.

4. Experimental Section

Film Growth: Epitaxial SRO films were grown on STO (001) substrates by reflection high energy electron diffraction (RHEED)-assisted pulsed laser deposition (PLD) using a 248 nm KrF excimer laser. The growth temperature, laser fluence, and oxygen partial pressure were 720 °C, 1 J cm^{-2}, and 100 mTorr, respectively. After deposition, the films were cooled at 10 K min^{-1} in an oxygen pressure of 100 Torr. For the tetragonal film growth, a lower oxygen pressure (1 mTorr) was used but otherwise the growth conditions were the same. The film thickness was determined from RHEED oscillations.

Device Fabrication: Conventional photolithography techniques were used to fabricate Hall bar devices. The SRO film was first etched to create a channel with an area of 65 × 30 μm^2 using argon ion beam sputtering (SCIA coat 200). Then, the sample was annealed in a tube furnace at 650 °C for 1 h in flowing oxygen to recover from any damage from the physical etching process. Au (70 nm)/Ru (5 nm) layers were then ion-beam sputter deposited to form electrical contact pads. Finally, Pt nanoparticles were deposited as a catalyst on the device using a sputter coater (AGB7340) for which the sputtering current, pressure, and time were 30 mA, 75 mTorr, and 12 s, respectively.

Hydrogen Spillover: For the hydrogenation of the Hall bar devices, the device with the Pt nanoparticles was wire-bonded on to a PPMS puck. Then, the puck was mounted in a specially designed gas box. The box was first flushed in flowing Ar gas, then the sample was heated in a flowing gas mixture of H_2 (5%) and Ar (95%). The sample resistance was measured during the hydrogenation process. After hydrogenation for 12 h at various temperatures, the sample was cooled down to room temperature. Finally, the puck was moved to the PPMS system within ≈10 min for low temperature transport measurements.

Electronic and Magnetic Property Measurements: The transport measurements were carried out in a physical property measurement system (PPMS) (Quantum Design). For the longitudinal and transverse resistance measurements, a constant current of 100 μA was applied using a Keithley 6221 current source, and the voltages were measured by Keithley 2182A nano-voltmeters. The temperature and magnetic-field-dependent magnetization was measured using a MPMS-3 SQUID (Superconducting Quantum Interference Device) magnetometer. Θ–2θ scans were performed using a Bruker D8 Discovery X-ray diffractometer with Cu K_α radiation.

XAS and XMCD studies of the pristine and hydrogenated SRO samples were carried out at the BOREAS beamline at the ALBA synchrotron light source (Barcelona, Spain).[55] This beamline allows for high-flux, high-resolution soft X-ray spectroscopy over a broad photon energy range (80–4000 eV) with full X-ray polarization control. The measurements were performed in a high-field cryomagnet in an ultrahigh vacuum chamber with a base pressure of ≈10^{-8} mTorr. The incoming X-ray beam was incident along a direction normal to the sample film surface under a 6 T magnetic field along the X-ray beam direction at 3 K. X-ray spectra across the O *K*-edge were acquired using a nearly 100% circularly polarized X-ray beam, while spectra for the Sr and Ru $L_{2,3}$-edges used 70% circularly polarized X-rays. XPS measurements were carried out using a Thermo Scientific K-Alpha instrument. The film surface was gently cleaned by Ar cluster ion etching prior to the measurements. Variable temperature MFM measurements were performed with an Attocube system (attoAFM I) incorporating a liquid helium based cryostat (attoLIQUID2000). MFM imaging of the magnetic textures was carried out using a magnetic tip from Nanosensors (SSS-QMFMR) in two steps. First, the topography of the sample was acquired after correcting for tilt and misalignment of the sample. Then, the tip was lifted from the sample surface to measure the magnetic signal and scanned at a fixed lift height (50–60 nm) in a phase modulation mode. All MFM measurements were carried out in vacuum (≈0.07 mTorr) with a high quality factor cantilever.

In Situ XRD Measurements: In situ XRD was carried out using synchrotron radiation at the 3D beamline of the Pohang Light Source-II (PLS-II). The sample was mounted in a heating chamber. Gas flow mixtures of 5% H_2 and 95% N_2 gas, and dry air formed from 21% O_2 and 79% N_2, were used for hydrogenation and dehydrogenation, respectively. In situ synchrotron surface X-ray diffraction crystal truncation rod (CTR) and half order reflection measurements were performed at both sector 12-ID-D and sector 33-ID-D of the Advanced Photon Source at Argonne National Laboratory. The CTR and half order reflections were measured using a Pilatus 100K area detector at an X-ray energy of 20 KeV. The scattering backgrounds were removed using the 2D area detector images. Geometric corrections and background subtractions were applied for all data. To elucidate the detailed atomic structures of ultrathin SRO film before and after hydrogenation, a set of specular and off-specular CTRs were measured and quantified using the COBRA method. The total structure factors from measured CTR intensities were able to determine the electron density distribution with sub-angstrom resolution using a Fourier transformation and iterative procedure. During in situ hydrogenation measurements, the SRO film was mounted in a gas flow sample cell using a flow of 3% H_2 + 97% Ar.

RBS Measurements: ERD spectroscopy using an NEC Pelletron Ion Accelerator was carried out to estimate the hydrogen content in the SRO thin films. Due to the natural hydrogen contamination on the film surface, we used deuterium gas (D_2) for the spillover process. ERD after the D_2 treatment was performed immediately after unloading the sample out of the gas cell, such that the sample was only in air for a few minutes before the ERD measurement. A 1.9 MeV He^+ beam with a current of 40 nA was utilized. The 5 × 3 mm^2 sample was measured in a high vacuum (≈10^{-4} mTorr) end station using a glancing incidence geometry. The incident and scattered beams were oriented within the horizontal plane at angles of 70° and 30°, respectively. Thus, the 2 mm diameter incident beam has an elliptical area of ≈4 × 2 mm^2 at the sample surface. To measure only the recoil particles and subtract any

scattered alpha particles, a filter formed from a 10 µm-thick Mylar foil is placed in front of the Ametec detector. A charge integration circuit is set to collect a 20 uC dose. The RBS is done in parallel with the ERD for elemental analysis and depth profiling of the sample. The RBS detector is placed immediately under the incidence beam at a 169° scattering angle. The RBS data is collected in a non-channeling geometry. A thick Kapton foil with a thin Au capping layer is used to calibrate the energy scale. Data processing is performed using the SimNRA 7.03 code. The RBS spectroscopy showed that there were $\approx 2.2 \times 10^{15}$ Pt atoms cm^{-2} on the SRO surface which is equivalent to ≈3 Å-thick Pt.

DFT Calculations: The DFT calculations were performed using a first-principles Green function method[56,57] within the density functional theory in a generalized gradient approximation.[58] The structure was adopted from the current experiments: pristine film (a = 3.905 Å, c = 3.9841 Å), tetragonal—relaxed (a = 3.905 Å, c = 4.000 Å), tetragonal—hydrogenated (a = 3.905 Å, c = 4.0297 Å), where it was assumed, in each case, that the in-plane lattice constants are clamped to the substrate. Disorder effects were simulated using both a virtual crystal approximation and a coherent potential approximation (CPA).[59] Both methods gave very similar results for H doped $SrRuO_3$ (SRO) so only results obtained within the virtual crystal approximation are included. Magnetic interactions were estimated using a magnetic force theorem implemented within multiple scattering theory.[60]

Supporting Information

Supporting Information is available from the Wiley Online Library or from the author.

Acknowledgements

This project has received funding from the European Union's Horizon 2020 research and innovation program under grant agreement No 737109. Funding has been provided by the Alexander von Humboldt Foundation in the framework of the Alexander von Humboldt Professorship to S.S.P.P. endowed by the Federal Ministry of Education and Research. The authors acknowledge the provision of beamtime at the ALBA synchrotron via proposals 2020094583 and 2021025037. M.V and C.G. acknowledge additional funding from grants PID2020-116181RB-C32 and FlagEra SOgraphMEM PCI2019-111908-2 (AEI/FEDER), and useful advice on Ru-L3,2 sum-rule analysis by Dr. S. Agrestini. This research used resources of the Advanced Photon Source, a U.S. Department of Energy (DOE) Office of Science user facility operated for the DOE Office of Science by Argonne National Laboratory under Contract No. DE-AC02-06CH11357. The authors thank the Pohang Light Source-II for use of the 3D beamline through Proposal No. 2019-3rd-3D-007. They also thank Holger L. Meyerheim for the discussion of structural data and Jae-Chun Jeon for the setup of the in situ transport measurement.

Open access funding enabled and organized by Projekt DEAL.

Conflict of Interest

The authors declare no conflict of interest.

Authors Contribution

H.H. and S.S.P.P. initiated the project. H.H. designed the in situ hydrogen spillover system and grew epitaxial thin films. H.H. and A.S. performed the transport measurements. H.H. carried out XRD, SQUID, XPS, and in situ synchrotron (PLS-II) measurements. H.Z. and Y.L. performed in situ synchrotron (APS) surface CTR measurements and analysis. M.V. and C.G. performed XAS/XMCD. A.K.S. performed MFM. I.K. carried out RBS and ERD. A.E. performed DFT calculations. H.H. was the lead researcher. S.S.P.P. supervised the project. H.H. and S.S.P.P. wrote the manuscript with input from all authors.

Data Availability Statement

The data that support the findings of this study are available from the corresponding authors upon reasonable request.

Keywords

anomalous Hall effect, hydrogenation, octahedral tilt, $SrRuO_3$, thin films

Received: August 9, 2022
Revised: September 18, 2022
Published online: November 20, 2022

[1] N. Nagaosa, J. Sinova, S. Onoda, A. H. MacDonald, N. P. Ong, *Rev. Mod. Phys.* **2010**, *82*, 1539.
[2] M. Dc, R. Grassi, J. Y. Chen, M. Jamali, D. Reifsnyder Hickey, D. Zhang, Z. Zhao, H. Li, P. Quarterman, Y. Lv, M. Li, A. Manchon, K. A. Mkhoyan, T. Low, J. P. Wang, *Nat. Mater.* **2018**, *17*, 800.
[3] K. Wang, Y. Zhang, G. Xiao, *Phys. Rev. Appl.* **2020**, *13*, 064009.
[4] Z. Fang, N. Nagaosa, K. S. Takahashi, A. Asamitsu, R. Mathieu, T. Ogasawara, H. Yamada, M. Kawasaki, Y. Tokura, K. Terakura, *Science* **2003**, *302*, 92.
[5] P. Bruno, V. K. Dugaev, M. Taillefumier, *Phys. Rev. Lett.* **2004**, *93*, 096806.
[6] A. Fert, N. Reyren, V. Cros, *Nat. Rev. Mater.* **2017**, *2*, 17031.
[7] T. Kurumaji, T. Nakajima, M. Hirschberger, A. Kikkawa, Y. Yamasaki, H. Sagayama, H. Nakao, Y. Taguchi, T. Arima, Y. Tokura, *Science* **2019**, *365*, 914.
[8] A. K. Nayak, V. Kumar, T. Ma, P. Werner, E. Pippel, R. Sahoo, F. Damay, U. K. Rossler, C. Felser, S. S. P. Parkin, *Nature* **2017**, *548*, 561.
[9] G. Koster, L. Klein, W. Siemons, G. Rijnders, J. S. Dodge, C.-B. Eom, D. H. A. Blank, M. R. Beasley, *Rev. Mod. Phys.* **2012**, *84*, 253.
[10] L. Wang, Q. Feng, Y. Kim, R. Kim, K. H. Lee, S. D. Pollard, Y. J. Shin, H. Zhou, W. Peng, D. Lee, W. Meng, H. Yang, J. H. Han, M. Kim, Q. Lu, T. W. Noh, *Nat. Mater.* **2018**, *17*, 1087.
[11] J. Matsuno, N. Ogawa, K. Yasuda, F. Kagawa, W. Koshibae, N. Nagaosa, Y. Tokura, M. Kawasaki, *Sci. Adv.* **2016**, *2*, e1600304.
[12] Y. Ohuchi, J. Matsuno, N. Ogawa, Y. Kozuka, M. Uchida, Y. Tokura, M. Kawasaki, *Nat. Commun.* **2018**, *9*, 213.
[13] Q. Qin, L. Liu, W. Lin, X. Shu, Q. Xie, Z. Lim, C. Li, S. He, G. M. Chow, J. Chen, *Adv. Mater.* **2019**, *31*, 1807008.
[14] K. Y. Meng, A. S. Ahmed, M. Bacani, A. O. Mandru, X. Zhao, N. Bagues, B. D. Esser, J. Flores, D. W. McComb, H. J. Hug, F. Yang, *Nano Lett.* **2019**, *19*, 3169.
[15] J. Lu, L. Si, Q. Zhang, C. Tian, X. Liu, C. Song, S. Dong, J. Wang, S. Cheng, L. Qu, K. Zhang, Y. Shi, H. Huang, T. Zhu, W. Mi, Z. Zhong, L. Gu, K. Held, L. Wang, J. Zhang, *Adv. Mater.* **2021**, *33*, 2102525.
[16] D. Zheng, Y. W. Fang, S. Zhang, P. Li, Y. Wen, B. Fang, X. He, Y. Li, C. Zhang, W. Tong, W. Mi, H. Bai, H. N. Alshareef, Z. Q. Qiu, X. Zhang, *ACS Nano* **2021**, *15*, 5086.
[17] D. Kan, T. Moriyama, K. Kobayashi, Y. Shimakawa, *Phys. Rev. B* **2018**, *98*, 180408.

[18] L. Wu, F. Wen, Y. Fu, J. H. Wilson, X. Liu, Y. Zhang, D. M. Vasiukov, M. S. Kareev, J. H. Pixley, J. Chakhalian, *Phys. Rev. B* **2020**, *102*, 220406.
[19] L. Wang, Q. Feng, H. G. Lee, E. K. Ko, Q. Lu, T. W. Noh, *Nano Lett.* **2020**, *20*, 2468.
[20] G. Kim, K. Son, Y. E. Suyolcu, L. Miao, N. J. Schreiber, H. P. Nair, D. Putzky, M. Minola, G. Christiani, P. A. van Aken, K. M. Shen, D. G. Schlom, G. Logvenov, B. Keimer, *Phys. Rev. Mater.* **2020**, *4*, 104410.
[21] G. Kimbell, P. M. Sass, B. Woltjes, E. K. Ko, T. W. Noh, W. Wu, J. W. A. Robinson, *Phys. Rev. Mater.* **2020**, *4*, 054414.
[22] L. Wysocki, L. Yang, F. Gunkel, R. Dittmann, P. H. M. van Loosdrecht, I. Lindfors-Vrejoiu, *Phys. Rev. Mater.* **2020**, *4*, 054402.
[23] B. Sohn, E. Lee, S. Y. Park, W. Kyung, J. Hwang, J. D. Denlinger, M. Kim, D. Kim, B. Kim, H. Ryu, S. Huh, J. S. Oh, J. K. Jung, D. Oh, Y. Kim, M. Han, T. W. Noh, B. J. Yang, C. Kim, *Nat. Mater.* **2021**, *20*, 1643.
[24] M. Jo, H. J. Lee, C. Oh, H. Yoon, J. Y. Jo, J. Son, *Adv. Funct. Mater.* **2018**, *28*, 1802003.
[25] X. Yao, K. Klyukin, W. Lu, M. Onen, S. Ryu, D. Kim, N. Emond, I. Waluyo, A. Hunt, J. A. Del Alamo, J. Li, B. Yildiz, *Nat. Commun.* **2020**, *11*, 3134.
[26] C. Oh, I. Kim, J. Park, Y. Park, M. Choi, J. Son, *Adv. Electron. Mater.* **2020**, *7*, 2000802.
[27] F. Zuo, P. Panda, M. Kotiuga, J. Li, M. Kang, C. Mazzoli, H. Zhou, A. Barbour, S. Wilkins, B. Narayanan, M. Cherukara, Z. Zhang, S. Sankaranarayanan, R. Comin, K. M. Rabe, K. Roy, S. Ramanathan, *Nat. Commun.* **2017**, *8*, 240.
[28] G. Rimal, C. Schmidt, H. Hijazi, L. C. Feldman, Y. Liu, E. Skoropata, J. Lapano, M. Brahlek, D. Mukherjee, R. R. Unocic, M. F. Chisholm, Y. Sun, H. Yu, S. Ramanathan, C.-J. Sun, H. Zhou, S. Oh, *Phys. Rev. Mater.* **2021**, *5*, L052001.
[29] Z. Li, S. Shen, Z. Tian, K. Hwangbo, M. Wang, Y. Wang, F. M. Bartram, L. He, Y. Lyu, Y. Dong, G. Wan, H. Li, N. Lu, J. Zang, H. Zhou, E. Arenholz, Q. He, L. Yang, W. Luo, P. Yu, *Nat. Commun.* **2020**, *11*, 184.
[30] Z. Zhang, D. Schwanz, B. Narayanan, M. Kotiuga, J. A. Dura, M. Cherukara, H. Zhou, J. W. Freeland, J. Li, R. Sutarto, F. He, C. Wu, J. Zhu, Y. Sun, K. Ramadoss, S. S. Nonnenmann, N. Yu, R. Comin, K. M. Rabe, S. Sankaranarayanan, S. Ramanathan, *Nature* **2018**, *553*, 68.
[31] Y. Zhou, X. Guan, H. Zhou, K. Ramadoss, S. Adam, H. Liu, S. Lee, J. Shi, M. Tsuchiya, D. D. Fong, S. Ramanathan, *Nature* **2016**, *534*, 231.
[32] H. Yoon, M. Choi, T. W. Lim, H. Kwon, K. Ihm, J. K. Kim, S. Y. Choi, J. Son, *Nat. Mater.* **2016**, *15*, 1113.
[33] J. Wei, H. Ji, W. Guo, A. H. Nevidomskyy, D. Natelson, *Nat. Nanotechnol.* **2012**, *7*, 357.
[34] J. Park, H. Yoon, H. Sim, S. Y. Choi, J. Son, *ACS Nano* **2020**, *14*, 2533.
[35] H. Yoon, Y. Kim, E. J. Crumlin, D. Lee, K. Ihm, J. Son, *J. Phys. Chem. Lett.* **2019**, *10*, 7285.
[36] N. Lu, P. Zhang, Q. Zhang, R. Qiao, Q. He, H. B. Li, Y. Wang, J. Guo, D. Zhang, Z. Duan, Z. Li, M. Wang, S. Yang, M. Yan, E. Arenholz, S. Zhou, W. Yang, L. Gu, C. W. Nan, J. Wu, Y. Tokura, P. Yu, *Nature* **2017**, *546*, 124.
[37] M. A. Hope, K. J. Griffith, B. Cui, F. Gao, S. E. Dutton, S. S. P. Parkin, C. P. Grey, *J. Am. Chem. Soc.* **2018**, *140*, 16685.
[38] Q. Lu, S. Huberman, H. Zhang, Q. Song, J. Wang, G. Vardar, A. Hunt, I. Waluyo, G. Chen, B. Yildiz, *Nat. Mater.* **2020**, *19*, 655.
[39] P. Liu, B. Lei, X. Chen, L. Wang, X. Wang, *Nat. Rev. Phys.* **2022**, *4*, 336.
[40] J. Jeong, N. Aetukuri, T. Graf, T. D. Schladt, M. G. Samant, S. S. P. Parkin, *Science* **2013**, *339*, 1402.
[41] H. Han, A. Sharma, H. L. Meyerheim, J. Yoon, H. Deniz, K. R. Jeon, A. K. Sharma, K. Mohseni, C. Guillemard, M. Valvidares, P. Gargiani, S. S. P. Parkin, *ACS Nano* **2022**, *16*, 6206.
[42] J. Jeong, N. B. Aetukuri, D. Passarello, S. D. Conradson, M. G. Samant, S. S. Parkin, *Proc. Natl. Acad. Sci. USA* **2015**, *112*, 1013.
[43] Z.-C. Wang, Z.-Z. Cui, H. Xu, X.-F. Zhai, Y.-L. Lu, *Chin. Phys. B* **2019**, *28*, 087303.
[44] B. T. Thole, P. Carra, F. Sette, G. van der Laan, *Phys. Rev. Lett.* **1992**, *68*, 1943.
[45] M. Ishfaq, M. Rizwan Khan, M. F. Bhopal, F. Nasim, A. Ali, A. S. Bhatti, I. Ahmed, S. Bhardwaj, C. Cepek, *J. Appl. Phys.* **2014**, *115*, 174506.
[46] M. Alhaddad, Z. I. Zaki, M. S. Amin, *J. Inorg. Organomet. Polym. Mater.* **2021**, *31*, 3760.
[47] A. M. Glazer, *Acta Crystallogr.* **1972**, *B28*, 3384.
[48] W. Lu, P. Yang, W. D. Song, G. M. Chow, J. S. Chen, *Phys. Rev. B* **2013**, *88*, 214115.
[49] W. Lu, W. D. Song, K. He, J. Chai, C.-J. Sun, G.-M. Chow, J.-S. Chen, *J. Appl. Phys.* **2013**, *113*, 063901.
[50] R. Gao, Y. Dong, H. Xu, H. Zhou, Y. Yuan, V. Gopalan, C. Gao, D. D. Fong, Z. Chen, Z. Luo, L. W. Martin, *ACS Appl. Mater. Interfaces* **2016**, *8*, 14871.
[51] F. Bern, M. Ziese, K. Dörr, A. Herklotz, I. Vrejoiu, *Phys. Status Solidi RRL* **2013**, *7*, 204.
[52] D. Kan, R. Aso, H. Kurata, Y. Shimakawa, *J. Appl. Phys.* **2013**, *113*, 173912.
[53] K. Samanta, M. Ležaić, S. Blügel, Y. Mokrousov, *J. Appl. Phys.* **2021**, *129*, 093904.
[54] C. Etz, I. V. Maznichenko, D. Böttcher, J. Henk, A. N. Yaresko, W. Hergert, I. I. Mazin, I. Mertig, A. Ernst, *Phys. Rev. B* **2012**, *86*, 064441.
[55] A. Barla, J. Nicolas, D. Cocco, S. M. Valvidares, J. Herrero-Martin, P. Gargiani, J. Moldes, C. Ruget, E. Pellegrin, S. Ferrer, *J. Synchrotron. Radiat.* **2016**, *23*, 1507.
[56] M. Geilhufe, S. Achilles, M. A. Kobis, M. Arnold, I. Mertig, W. Hergert, A. Ernst, *J. Phys.: Condens. Matter* **2015**, *27*, 435202.
[57] M. Hoffmann, A. Ernst, W. Hergert, V. N. Antonov, W. A. Adeagbo, R. M. Geilhufe, H. B. Hamed, *Phys. Status Solidi B* **2020**, *257*, 1900671.
[58] J. P. Perdew, K. Burke, M. Ernzerhof, *Phys. Rev. Lett.* **1996**, *77*, 3865.
[59] B. L. Gyorffy, *Phys. Rev. B* **1972**, *5*, 2382.
[60] A. I. Liechtenstein, M. I. Katsnelson, V. P. Antropov, V. A. Gubanov, *J. Magn. Magn. Mater.* **1987**, *67*, 65.